CrossMark

Reconnection-generated Plasma Flows in the Quasi-separatrix Layer in Localized Solar Corona

Sripan Mondal[1], Abhishek K. Srivastava[1] , Sudheer K. Mishra[2], K. Sangal[1] , Pradeep Kayshap[3] , Yang Guo[4] ,
David I Pontin[5] , Vadim M. Uritsky[6] , Leon Ofman[6,7] , Tongjiang Wang[6] , and Ding Yuan[8]

[1] Department of Physics, Indian Institute of Technology (BHU), Varanasi-221005, India; asrivastava.app@iitbhu.ac.in
[2] Indian Institute of Astrophysics, Kormangala, Bangalore, India
[3] Vellore Institute of Technology (VIT) Bhopal, 466114, India
[4] School of Astronomy and Space Science, Nanjing University, People's Republic of China
[5] School of Information and Physical Sciences, University of Newcastle, Australia
[6] Catholic University of America and NASA-GSFC, USA
[7] Visiting, Tel Aviv University, Israel
[8] Institute of Space Science and Applied Technology, Harbin Institute of Technology, Shenzhen 518055, People's Republic of China

Abstract

Multiwavelength observations of the propagating disturbances (PDs), discovered by Atmospheric Imaging Assembly (AIA) on board Solar Dynamics Observatory (SDO), are analyzed to determine their driving mechanism and physical nature. Two magnetic strands in the localized corona are observed to approach and merge with each other, followed by the generation of brightening, which further propagates in a cusp-shaped magnetic channel. Differential emission measure analysis shows an occurrence of heating in this region of interest. We extrapolate potential magnetic field lines at coronal heights from the observed Helioseismic and Magnetic Imager vector magnetogram via Green's function method using MPI-AMRVAC. We analyze the field to locate magnetic nulls and quasi-separatrix layers (QSLs), which are preferential locations for magnetic reconnection. Dominant QSLs including a magnetic null are found to exist and match the geometry followed by PDs; therefore, this provides conclusive evidence of magnetic reconnection. In addition, spectroscopic analysis of Interface Region Imaging Spectrograph Si IV λ1393.77 line profiles show a rise of line width in the same time range depicting the presence of mass motion in the observed cusp-shaped region. PDs are observed to exhibit periodicities of around 4 minutes. The speeds of PDs measured by the surfing transform technique are close to each other in four different SDO/AIA bandpasses, i.e., 304, 171, 193, and 131 Å, excluding the interpretation of PDs in terms of slow magnetoacoustic waves. We describe comprehensively the observed PDs as quasiperiodic plasma flows generated as a result of periodic reconnection in the vicinity of a coronal magnetic null.

Unified Astronomy Thesaurus concepts: Solar corona (1483); Solar magnetic reconnection (1504); Solar coronal transients (312)

Supporting material: animations

1. Introduction

The corona, the outermost part of the solar atmosphere, is known to sustain a very high temperature (roughly of the order of megakelvin (MK)) compared to the inner layers. The corona drains out its energy through thermal conduction, through solar wind outflow, and via radiation to the surroundings. Therefore, in order to sustain the high temperature, the corona must be subjected to continuous heating, with possible mechanisms such as by dissipation of Alfvén waves (van Ballegooijen et al. 2011; Srivastava et al. 2017; Van Doorsselaere et al. 2020) and small-scale energy release events such as nanoflares (Parker 1988) as a manifestation of magnetic reconnection. Several energy dissipation mechanisms, such as resonant absorption (Ionson 1978) and phase mixing (Heyvaerts & Priest 1983), have been proposed through which wave heating may take place.

As per the coarser definition, the magnetic reconnection is a breaking and reconfiguration of oppositely directed magnetic field lines in highly conducting plasma via the formation of extended magnetic singularities in the form of a current sheet (i.e., localized region with high current density resulting from a steep gradient of the magnetic field over a short length scale) either associated with MHD instabilities (Baty 2000; Vekstein 2017) or triggered by external perturbations (Hahm & Kulsrud 1985; Srivastava et al. 2019, 2021). Magnetic reconnection is able to release magnetic energy stored in the large-scale magnetic field, hence serving to relieve the stress in a nonpotential field. The field lines coming into the current sheet region are referred to as reconnection inflows, while the reconfigured field lines dragging plasma with them as they exit outside the diffusion region are observed to move away as outflows (Priest & Forbes 2007). Magnetic reconnection has several effects like conversion of magnetic energy into heat via ohmic dissipation, acceleration of plasma by generating bulk kinetic energy from magnetic energy, generation of shock waves, turbulence, filamentation of currents, etc. (Pontin & Priest 2022). Magnetic reconnection is essentially a three-dimensional process that is classically linked to the presence of null points, where magnetic field vanishes whenever it is studied in the two-dimensional regime (Lau & Finn 1990; Wang 1997). Actually, the magnetic forces in the

neighborhood of magnetic nulls are not sufficient to withstand large variations of the magnetic stress and therefore result in the collapse of magnetic topology followed by the generation of current singularities (in ideal plasma conditions) and magnetic reconnection (Priest & Titov 1996). Although this classical explanation provides a fair enough idea about the magnetic reconnection process, still it is not sufficient while looking for reconnection scenarios in the presence of complex magnetic geometries in the real 3D solar atmosphere.

For example, in the context of the solar atmosphere, magnetic reconnection may take place along those parts of the photospheric polarity inversion lines where field lines meet the photosphere (known as bald patches) and form current singularities as a result of those attachments (Aly & Amari 1989; Vekstein et al. 1991). In 3D, the magnetic topology associated with magnetic nulls contains a spine axis and a fan plane. The straight field lines that are directed away or toward the null are collectively termed as the spine. The surface made up of field lines radiating or spiraling around nulls is defined as the fan plane. Depending on the radial or spiral nature of field lines in the fan plane, these nulls are categorized into radial and spiral types (Greene 1988; Parnell et al. 1996, 1997). The presence of radial nulls has been reported with a few spacecraft observations (Liu et al. 2018; Chen et al. 2019) and therefore confirms their existence in the diffusion regions. On the other hand, spiral nulls are rarely investigated in the diffusion region (Fu et al. 2017). In addition, reconnection can occur along separators, which are the intersections of separatrices or separatrix layers (SLs, i.e., the layers across which magnetic field lines show discontinuity in their connectivity; Priest 1996; Forbes 2000; Galsgaard et al. 2000). Démoulin et al. (1997) discussed that all the solar flare events could not be elucidated by topological features such as magnetic nulls, separators, and bald patches. Hence, these classes of topological features need to be extended on the basis of the concept of magnetic field line connectivity.

Therefore, a more generalized concept has been established that magnetic field lines subject to a drastic change of connectivity form the foundation of current accumulation even if no magnetic nulls are present there (Longcope & Strauss 1994). Priest & Démoulin (1995) termed the flux tubes exhibiting such behavior as quasi-separatrix layers (QSLs). For proper detection of QSLs, the squashing factor (Q) has been measured for elemental flux tubes of infinitesimal cross sections that connect opposite polarities at the photospheric level (Titov et al. 2002). As far as observational consequences of the presence of QSLs are concerned, plage brightenings and flare kernels in an X1 flare were located at the intersection of QSLs with the photosphere (Gaizauskas et al. 1998). Moreover, electric currents were found to be concentrated along the boundaries of QSLs. It has been inferred that when the thicknesses of QSLs and current layers associated with them are sufficiently small for reconnection to take place, the magnetic energy stored within QSLs will be released (Démoulin et al. 1997; Mandrini et al. 1997). Therefore, QSLs are treated as preferential regions for the increment of current density and the occurrence of magnetic reconnection even in the absence of magnetic nulls and bald patches (Milano et al. 1999; Aulanier et al. 2005; Titov et al. 2008).

In recent high-resolution, extreme-ultraviolet (EUV), on-disk observations, the propagating disturbances (PDs), i.e., translational movements of spatially localized intensity enhancements become inevitable observational scenarios in the solar atmosphere (DeForest & Gurman 1998; O'Shea et al. 2007; Gupta et al. 2012). The spectroscopic signatures of plasma flows are also observed using various spectrometers or spectrographs in different magnetic structures in the solar atmosphere (Harra et al. 2008; Dadashi et al. 2011; Srivastava et al. 2014; Kayshap et al. 2015; Rao et al. 2019). Apart from gentle plasma flows coupling different layers of the solar atmosphere, some of them may be linked with the impulsive transients or explosive events in the solar atmosphere (De Pontieu et al. 2011; Chen et al. 2019; Srivastava et al. 2020). To understand the underlying physical mechanism of these PDs or impulsive plasma flows, understanding of their morphological and thermodynamical properties, accurate estimations of propagation speeds and any inherent periodicities, and elaboration of magnetic topology or magnetic structure are essential.

Ofman et al. (1997) and DeForest & Gurman (1998) reported the first observations of intensity perturbations along solar coronal plumes, which they inferred to be slow magnetoacoustic waves. After this discovery, the presence of slow mode waves was reported in both closed and open loop topologies using data from several instruments and various data analysis procedures and simulation techniques (De Moortel et al. 2000; Banerjee et al. 2001; Marsh et al. 2009; Wang et al. 2009; Kiddie et al. 2012; Krishna Prasad et al. 2012; Kumar et al. 2013, 2015; Nisticò et al. 2017). Ofman et al. (2012) used a 3D MHD model to show the generation of slow magnetoacoustic waves in coronal loops by impulsive flows. Cho et al. (2021) investigated propagating intensity disturbances in five plumes and found that the PDs had higher propagation speeds in hot Atmospheric Imaging Assembly (AIA) channels, i.e., 193 and 211 Å, than that in the cooler 171 Å channel. The observed speed ratio between 171 and 193 Å channels had an estimated value of 1.3, which was close to the theoretical value (1.25) of slow magnetoacoustic waves. Li et al. (2018) observed disturbances originating from the reconnection region between closed coronal loops and overlying open loops, which propagate upward across the magnetic dip of the overlying loops with a mean speed of 200 km s^{-1}. They suggested that these disturbances are essentially the quasiperiodic magnetoacoustic waves.

On the other hand, depending on observation of time-varying blueward asymmetry in spectroscopic Hinode/EUV Imaging Spectrometer (EIS) observations, the observed intensity oscillations were inferred to be caused by quasiperiodic plasma upflows instead of slow-mode waves (De Pontieu & McIntosh 2010; Tian et al. 2011). McIntosh et al. (2010) interpreted propagating perturbations along polar plumes as quasiperiodically driven high-velocity outflows. Su et al. (2012) inferred that quasiperiodic pulsations (QPPs) propagating along a cusp-shaped loop formed after a flare are mostly episodic outflows rather than slow magnetoacoustic waves since they have almost the same propagation speed irrespective of formation temperatures. Pucci et al. (2014) found that the apparent speed of 30–300 km s^{-1} is higher in the low-temperature channel AIA 171 Å than those in high-temperature channels AIA 193 and 211 Å and hence interpreted PDs as plasma outflows.

Ning & Guo (2014) explored the moving bright structures along a magnetic loop connecting a pair of negative and positive fields during a coronal bright point (CBP) event having a lifetime of around 20 minutes. The average apparent speed of

the moving structures was found to be about 380 km s^{-1}, along with periodicity between 80 and 100 s. In addition to the observation, nonlinear force-free field extrapolation has been performed, which showed the possibility of magnetic reconnection taking place during the CBP. In addition, they interpreted those moving bright structures as observational outflows after commencement of magnetic reconnection in a CBP. Later, Li et al. (2016) also reported a similar kind of event and inferred that the moving structures are observational outflows after the onset of magnetic reconnection. Baker et al. (2009) linked Hinode EIS and XRT observations of AR 10942 with magnetic field modeling. They found that the observed outflows, having speeds of a few to 50 km s^{-1}, originate in the vicinity of QSLs, where magnetic field lines were showing a drastic change in the connectivity over a very thin volume. They inferred that magnetic reconnection at QSLs located between the closed field lines of an active region (AR) and large-scale externally connected field lines act as a driver of the observed active region outflows.

In the present paper, we describe the generation and propagation of quasiperiodic plasma flows from an elongated cusp-shaped region, which matches geometrically with QSLs. Detailed multiwavelength imaging (SDO/AIA), differential emission measure (DEM), magnetic field extrapolation and its topology analysis (nulls and QSLs), spectroscopic observations (IRIS Si IV line), and wavelet and surfing transform techniques (Uritsky et al. 2013) are extensively utilized to draw a detailed physical picture of the merging of two extended, curved bundles of magnetic field lines indicative of magnetic flux tubes, onset of reconnection in QSLs or SLs (which also includes magnetic null), and generation of quasiperiodic plasma flows. In Section 2, the observational scenario and data (SDO/AIA, SDO/HMI, IRIS/SJI, IRIS/Si IV spectra) associated with the present scientific work, as well as methods used for preprocessing of them before further analysis, are presented. In Section 3, the observational (imaging as well as spectroscopic) results and magnetic topology analysis are reported and discussed in a sequential manner. In Section 4, we summarize our new scientific findings and draw conclusions.

2. Observational Data and Their Overview

SDO/AIA, with its multiwavelength imaging capability of the full solar disk, investigates various dynamics (e.g., reconnection, outflows, inflows) happening over small to large spatial length scales in different atmospheric layers. It has a spatial resolution of 1″5 and a temporal cadence of 12 s in all of its EUV filters: 94 Å (Fe X, Fe XVIII, $T \approx 1$ MK, $T \approx 6.3$ MK), 131 Å (Fe VIII, Fe XXI, Fe XXIII, $T \approx 0.4$, 10, 16 MK), 171 Å (Fe IX, $T \approx 0.7$ MK), 193 Å (Fe XII, Fe XXIV, $T \approx 1.2$, 20 MK), 211 Å (Fe XIV, $T \approx 2$ MK), 304 Å (He II, $T \approx 0.05$ MK), and 335 Å (Fe XVI, $T \approx 2.5$ MK) (Lemen et al. 2012). The data analyzed here are observed by AIA within the spatial extent of $X = [420″, 500″]$ and $Y = [-280″, -180″]$ from 18:40 UT to 19:45 UT on 2021 April 17. We exported level 1.0 data for all EUV AIA wavelengths from the Joint Science Operations Center (JSOC),[9] which were already preprocessed to make corrections such as removal of dark current, de-spiking, flat-fielding, and bad-pixel removal. Then, using information such as CRPIXi, CDELTi (for $i = 1$ or 2), etc., from FITS headers of AIA files, those level 1.0 data were again

processed to co-align all images in different wavelengths to a common center, to correct the roll angles, and to rescale images to a common plate scale using the Solarsoft (Freeland & Handy 1998) IDL routine "aia_prep.pro." Likewise, the Helioseismic and Magnetic Imager (HMI), having a spatial resolution of 1″0, provides maps of the line-of-sight (LOS) component of magnetic field with a temporal cadence of 45 s and maps of vector magnetic field with a temporal cadence of 720 s of the entire disk at the photospheric level (Scherrer et al. 2012). We used "hmi_prep.pro" to co-align HMI and AIA data.

We also used spectral data from NASA's Interface Region Imaging Spectrograph (IRIS) spacecraft (De Pontieu et al. 2014), which observes the lower solar atmosphere (chromosphere and transition region). The IRIS spacecraft observes the Sun in far-ultraviolet (FUV: 1331.56–1358.40 Å and 1390.00–1406.79 Å) and near-ultraviolet (NUV: 2782.56–2833.89 Å) wave bands using slit jaw imagers (SJIs). The IRIS spacecraft also provides spectroscopic observations for some notable bright lines in the NUV region, e.g., C II λ1334.53, C II λ1335.66, Si IV λ1393.77, and Si IV λ1402.77, and in the FUV region, such as Mg II k λ2796 and Mg II h λ2803. The IRIS observation occurred between 17:00 and 23:00 UT on 2021 April 17. However, we used only Si IV λ1393.77 spectral data in a short time interval of 19:13–19:30 UT, where the reconnection appears to take place. A large coarse eight-step raster scan with a temporal cadence of 5 s is used in the analysis; therefore, each raster scan takes $5.0 \times 8 = 40$ s. The IRIS field of view (FOV) is 120″ × 119″ centered at 449″ in the x-direction and −266″ in the y-direction.

The evolution of two curved, elongated features indicative of magnetic flux tubes approaching each other, and therefore merging to generate propagating brightness, is primarily evident in AIA temporal images (Figures 1 and 2). The evolution of plasma in the surroundings associated with enhanced DEM (i.e., greater electron number density at higher temperatures), as well as generation and propagation of brightness, are observed and studied in greater details in the considered event using time-series of various AIA EUV filters as described in Section 3. A composite image of AIA 171, 131, and 193 Å around 19:18 UT (top left panel), along with images with a small field of view (right panels) showing brightened field lines (elongated inverted Y-shaped topology) in 304, 171, 193, 211, and 131 Å, is shown in Figure 1. To make the elongated inverted Y-shaped topology more clearly evident, the structure is demonstrated by green lines overplotted on the image of 211 Å. In addition, images in 335 Å and 94 Å (not shown here) contain a clear signature of the hot cusp-shaped region; however, extended magnetic legs are not properly visible in these images. The HMI magnetogram at time 19:24 UT is also shown with a magenta rectangular box enclosing the area of interest. It is evident that the region of interest (ROI) is just above a plage region having strong opposite polarities associated with it.

3. Results

In the time span between 18:56 UT and 19:03 UT, nonperiodic faint plasma upflows having speeds of 75 and 97 km s^{-1} were observed to move toward the top of the cusp region along the left magnetic segment (which is covered by a slit shown by green dashed lines from a to b in the left panels of
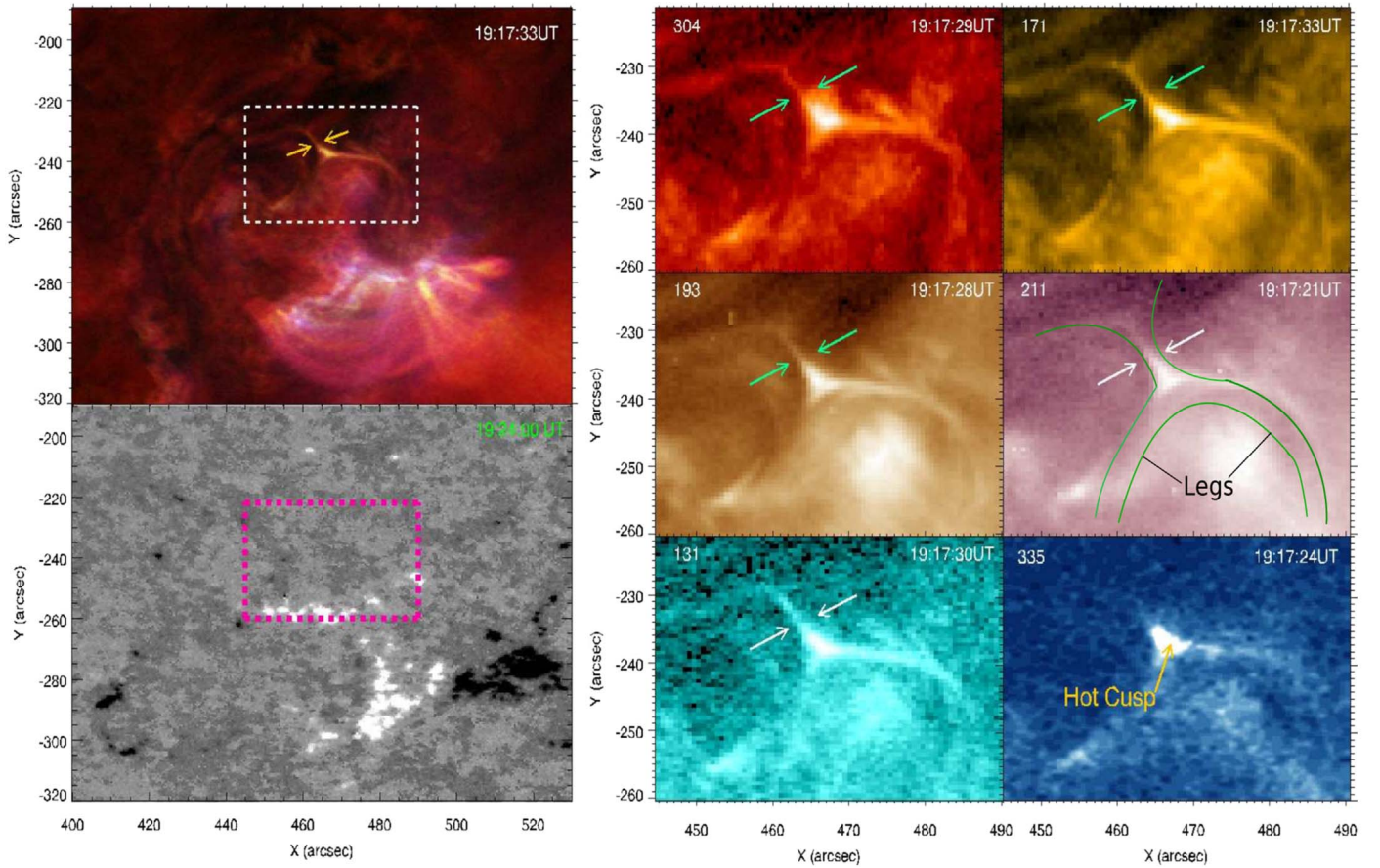
---

[9] http://jsoc.stanford.edu/

Figure 1. Top left panel: a composite image of AIA 171, 131, and 193 Å is shown with a larger field of view, with the white box drawn to demonstrate the more specific FOV of the considered event. Emissions at wavelengths 171, 131, and 193 Å are respectively represented by pseudo-colors golden-yellow, greenish-blue, and brown. Bottom left panel: the HMI magnetogram corresponding to the same FOV (magenta box) is shown. Right panels: small FOV images in six AIA wavelengths, i.e., 304, 171, 193, 211, 131, and 335 Å, are presented. The elongated curved cusp-like magnetic structure under consideration is shown by green curves overplotted on the 211 Å image. The top part of this cusp-shaped structure is basically the magnetic channel where quasiperiodic plasma flow occurred. Although the extended curved field line is not visible properly in 335 Å, the hot cusp-shaped region is clearly evident.

Figure 3) as evident in the distance–time map in the right panels of Figure 3.

Just after those upflows, around 19:03 UT, two curved, elongated features indicative of magnetic flux tubes were seen to approach each other as indicated by yellow arrows overplotted on the composite images of 171, 193, and 131 Å in Figure 2 (see online animation related to Figure 2). Thereafter an extended inverted Y-shaped magnetic geometry was found to be formed in the surroundings (the detailed analysis of magnetic topology is given in Section 3.1.2). We term its upper part as an elongated cusp-shaped region, while its downward part is the curved and closed loop-like structure. Around 19:09 UT, the elongated cusp-shaped portion of this magnetic structure was brightened, which we termed as an apparent current sheet where reconnection might take place (see the online animation associated with Figure 2). Thereafter, additional brightness was seen to originate at the top region of this elongated straight portion. The brightness propagated downward in the elongated cusp-shaped region and thereafter moved through the rightward magnetic channel. This generation of brightness and its propagation through that segment were observed almost continuously from 19:12 UT to 19:28 UT, before the structure disappeared (see online animation related to Figure 2).

To study the physical scenario associated with these propagating intensity features (termed as PDs hereafter) and the nature of these features, we compute the DEM and magnetic structure in Section 3.1, and we measure the period and propagation speeds at different wavelengths in Section 3.2.

3.1. Physical Scenario of the Region Associated with Propagating Disturbances

We conjecture that PDs were generated as a result of magnetic reconnection, as two magnetic flux tubes were clearly seen to approach each other and thereafter merge with each other just before the brightening was started. To examine whether magnetic reconnection is possible in this region, and therefore to provide conclusive support to our primary observational findings as shown in Figures 1 and 2 about triggering of PDs, we tried to find out whether any heating was taking place in the considered region via DEM analysis (see Section 3.1.1). In addition, magnetic field extrapolation has been carried out for finding magnetic field topology in the ROI, and thereafter that field topology was analyzed to locate magnetic nulls, as well as QSLs, as they are considered to be the preferential locations for an occurrence of magnetic reconnection (see Section 3.1.2).
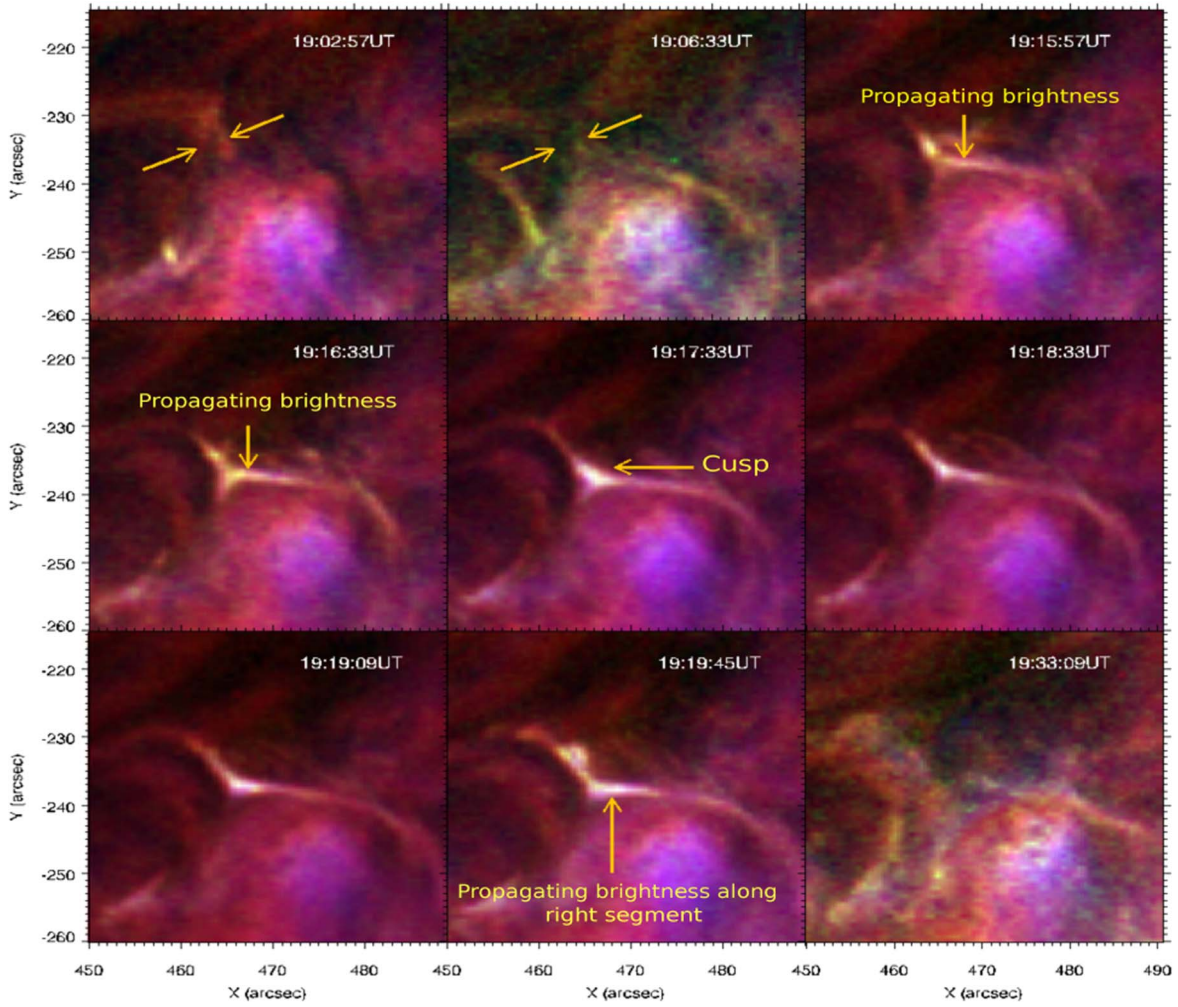
Figure 2. Composite image of 171, 131, and 193 Å showing temporal evolution of the event under consideration. Emissions at wavelengths 171, 131, and 193 Å are respectively represented by pseudo-colors golden-yellow, greenish-blue, and brown. At first, two curved, elongated magnetic flux tubes are seen to approach each other around 19:02 UT, followed by formation of an apparent current sheet around 19:15 UT. Thereafter, a prominently visible bright Y-shape structure is formed around 19:16 UT. Brightenings are observed to be originated at the cusp-shaped region as shown in rightmost part of the middle panel. It propagates downward and then keeps traversing prominently in the right leg of this Y-shape structure. Around 19:33 UT, the structure disappears. The entire dynamics happening in the time interval 18:48–19:33 UT, with temporal cadence being 12 s, is shown in the animation. The real-time animation duration is 22 seconds.

(An animation of this figure is available.)

3.1.1. Differential Emission Measure Analysis and Heating

We studied thermal structures of plasma flows via DEM analysis. We used the sparse inversion method as described by Cheung et al. (2015) to estimate DEM at temperatures $\log T = 5.6$–7.4 using six AIA filters, i.e., 94, 131, 171, 193, 211, and 335 Å. The total emission measure (EM) from the specified temperature interval, ΔT, is

$$\mathrm{EM}_T = \mathrm{DEM}(T)\Delta T = \int_0^\infty n_e^2(T)\, dl,$$

quantifying the thermal characteristics of the plasma integrated over the portion of the LOS (along the length element dl) per unit area on which the temperature is between T and $T + \Delta T$. Parameter $n_e(T)$ is the electron number density of the plasma at a certain temperature T (Cheung et al. 2015). Since DEM is proportional to n_e^2, it is considered as a proxy for studying the evolution of the number density of electrons. In addition,

DEM-weighted temperature was estimated in log scale using

$$\frac{\sum_{i=1}^{n} (\mathrm{DEM}_i \times \log T_i)}{\sum_{i=1}^{n} \mathrm{DEM}_i},$$

where i stands for different temperature bins of width $\Delta \log T = 0.1$ and n is the total number of temperature bins.

We took a rectangular box (smaller box shown in the DEM map for $\log T = 7.1 - 7.4$) of spatial extent $x = [467'', 472'']$ and $y = [-235'', -229'']$ covering the top of the elongated cusp-shaped region from where the brightness originated. The thermal nature of the considered event in different temperature ranges within $\log T = 5.6 - 7.4$ is shown in the top panel of Figure 4 (see online animation also). The temporal evolution of total EM and DEM-weighted temperature are shown in the bottom panel of Figure 4. It is evident that both of them show a rise starting around 19:12 UT and further peaks around 19:21 UT, and thereafter they continue to decay. Since EM is proportional to the square of plasma number density, an
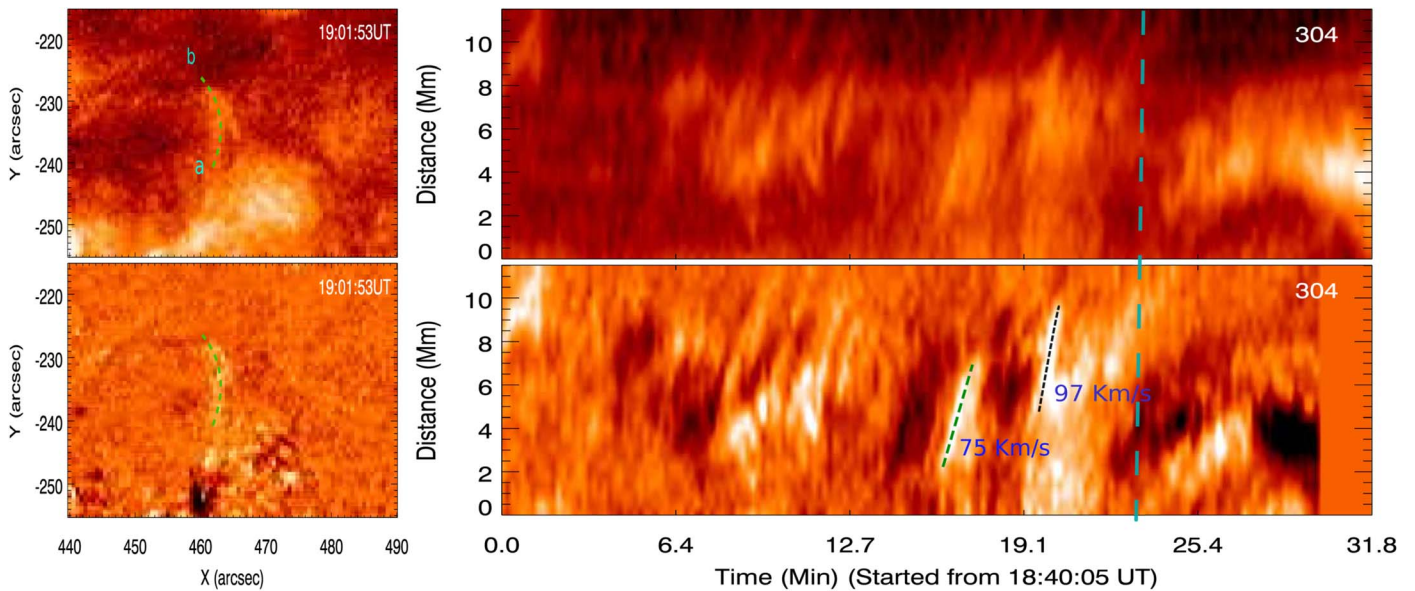
Figure 3. Left panels: slit orientation overplotted as a green dashed line from a to b on the AIA 304 Å image (top: normal intensity; bottom: running difference, with time difference being 2 minutes) having spatial extent $X = [440'', 490'']$, $Y = [-255'', -215'']$ for capturing the preexisting plasma upflows observed to propagate upward from the left magnetic channel to the elongated cusp-shaped region subsequently filling the mass there. Right panels: distance–time maps (top: normal intensity; bottom: running difference) provide evidence of flows with speeds of 75 and 97 km s^{-1}. These speeds were estimated by the slopes of straight line fits along tilted bright fronts in a running-difference distance–time map. The vertical dashed cyan line denotes the approximate onset time of the merging of flux tubes and hence clearly differentiates this upflow from the reconnection-generated plasma flows.

increase in EM may result from the increment of high-temperature plasma within the ROI, i.e., in the elongated cusp-shaped region and in the downward magnetic channel (Figure 4).

Now the instantaneous presence and increment of high-temperature plasma can be due to either of two reasons or both, i.e., (i) some amount of plasma is already present there and gets heated by some mechanism (e.g., energy release due to reconnection), and (ii) high-temperature plasma is flowing into that region in due course of time, due to thermal conduction and evaporation of chromospheric plasma. We already observed faint plasma flows (prominently visible in cool AIA filter, i.e., 304 Å) propagating upward along the left segment of the concerned magnetic structure to the ROI around 18:56–19:03 UT as discussed in Figure 3.

However, no flows were observed to enter in that region after that particular time during the main epoch of the event (19:10 UT–19:28 UT). Therefore, the rise in the EM and temperature could not be caused by that particular upflow through the left segment and rather resulted from heating of the plasma already present or filled there.

It is to be noted that there is a certain limitation of inversion methods used to estimate DEM using AIA filters alone: it does not provide pinpoint accuracy in the estimation of EM in higher-temperature bins for broader DEMs, i.e., for the multithermal plasma, as AIA temperature response functions do not constrain higher-temperature plasma accurately (Guennou et al. 2012; Cheung et al. 2015). However, in this work our objective is to demonstrate the evolution of multitemperature plasma contained within the considered structure during the magnetic reconnection process. We do not aim to estimate the exact amount of heating that occurred in the evolved plasma to match it with the the excessive appearance of emitting plasma in high-temperature AIA filters. Instead, we only aim to show that there is an occurrence of some amount of heating to show that magnetic reconnection is an ongoing process that causes

evolution of heated multitemperature plasma flowing quasiperiodically in the concerned magnetic structure. Therefore, even if DEMs in high temperature are not well constrained, still it is clearly visible in higher-temperature DEM maps that initially high-temperature plasma was absent in the reconnection region, and as reconnection sets in, they start to appear, providing evidence of heating there (see Figure 4).

Therefore, we infer that formation of an X-type structure apparently seen in 2D AIA images and merging of two flux tubes just before the increments in both these quantities display a connection between onset of magnetic reconnection and thereby possible heating and evolution of high-temperature plasma.

3.1.2. Measurements of Magnetic Field and Associated Magnetic Nulls and QSLs

In order to explore the occurrence of magnetic reconnection with more conclusive evidence, we extrapolated magnetic field lines at coronal heights and tried to identify the presence of magnetic nulls/QSLs.

(I) *Potential field extrapolation*. The direct observation of magnetic field is only available at the photospheric level. Therefore, we used the potential field extrapolation technique applying Green's function method (Chiu & Hilton 1977) to obtain magnetic field topology in the surroundings of our ROI located in the solar corona. The HMI (Scherrer et al. 2012; Schou et al. 2012) vector magnetograms ("hmi.B_720s" series) of temporal cadence 720 s were taken as our lower boundary conditions. Since the transverse components of those magnetograms were subjected to 180° ambiguity, magnetograms were corrected by removing this ambiguity using the minimum energy method as implemented in the HMI pipeline (Metcalf 1994; Metcalf et al. 2006; Leka et al. 2009). Since the ROI was far away from the disk center, the magnetograms were further corrected for the projection effect by the method
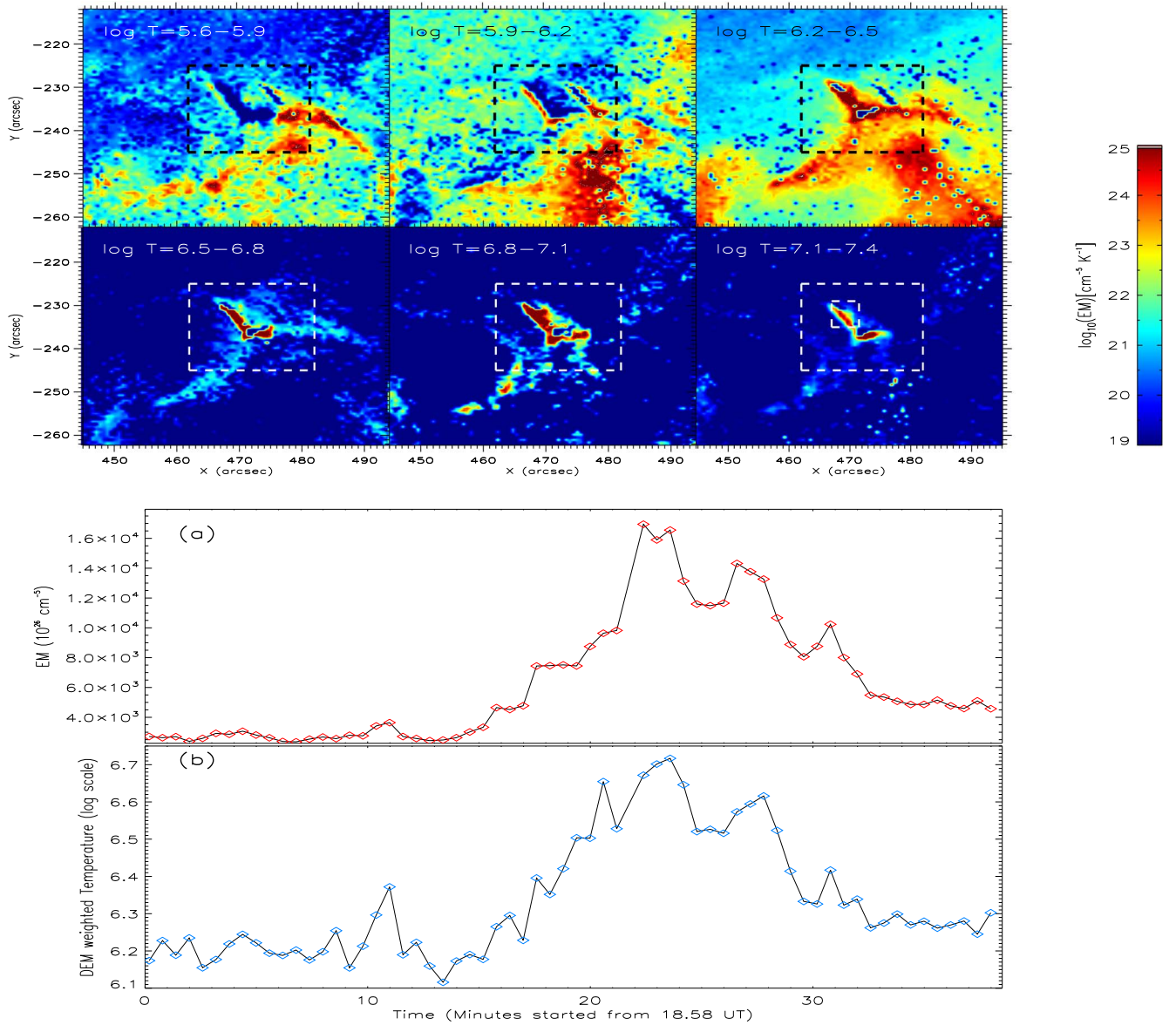
Figure 4. Top panel: DEM maps at six different temperature ranges between log $T = 5.6$ and 7.4 at time 19:21 UT. Rectangular boxes are used to specify a more exact location of the considered event, i.e., brightening in an inverted Y-shape structure. Bottom panel: (a) temporal evolution of the total EM; (b) evolution of DEM-weighted temperature with time covering our considered event evaluated from the region enclosed by the smaller rectangular box shown in DEM for log $T = 7.1$–7.4. The thermal evolution of this structure and its surroundings from 18:50 UT to 19:36 UT with temporal cadence of 36 s is shown in the animation containing maps from all six temperature ranges shown in the top panel of this figure. The real-time animation duration is 7 seconds.

(An animation of this figure is available.)

described in Gary & Hagyard ([1990](#)). Basically, the magnetogram data taken from JSOC are in the helioprojective Cartesian coordinate system. So we deprojected it to the heliographic coordinate system. It was basically a two-step procedure. First, the components of vector magnetic fields in the helioprojective plane were transformed to heliographic components on the same helioprojective plane. Afterward, the helioprojective plane was transformed to a local plane tangent to the solar surface at the center of the ROI. Since the geometry of the field of view suffered change as a result of removing the projection effect, we recut the edges to get a rectangular boundary of the magnetogram enclosing ROI. The extrapolated area was resolved by 244×132 grid points, with the coarsest spatial resolution in both the x- and y-directions being $2''$. In addition, the force-free and torque-free conditions are usually not

satisfied for the observed magnetic field, and therefore a preprocessing method (Wiegelmann et al. [2006](#)) was taken into account to remove the net force and torque on the bottom boundary of the computational domain used for the extrapolation. The preprocessed magnetograms were used to extrapolate potential coronal magnetic field in the MPI-Adaptive Mesh Refinement-Versatile Advection Code (MPI-AMRVAC;[10] Keppens et al. [2012](#), [2021](#); van der Holst et al. [2012](#); Porth et al. [2014](#); Xia et al. [2018](#)). Previous applications could be found in Guo et al. ([2013](#)), Yang et al. ([2015](#)), and Guo et al. ([2017](#)). The extrapolated field lines showed that there were multiple small-scale loops at lower heights in the inner corona, and there were a few comparably elongated field lines that
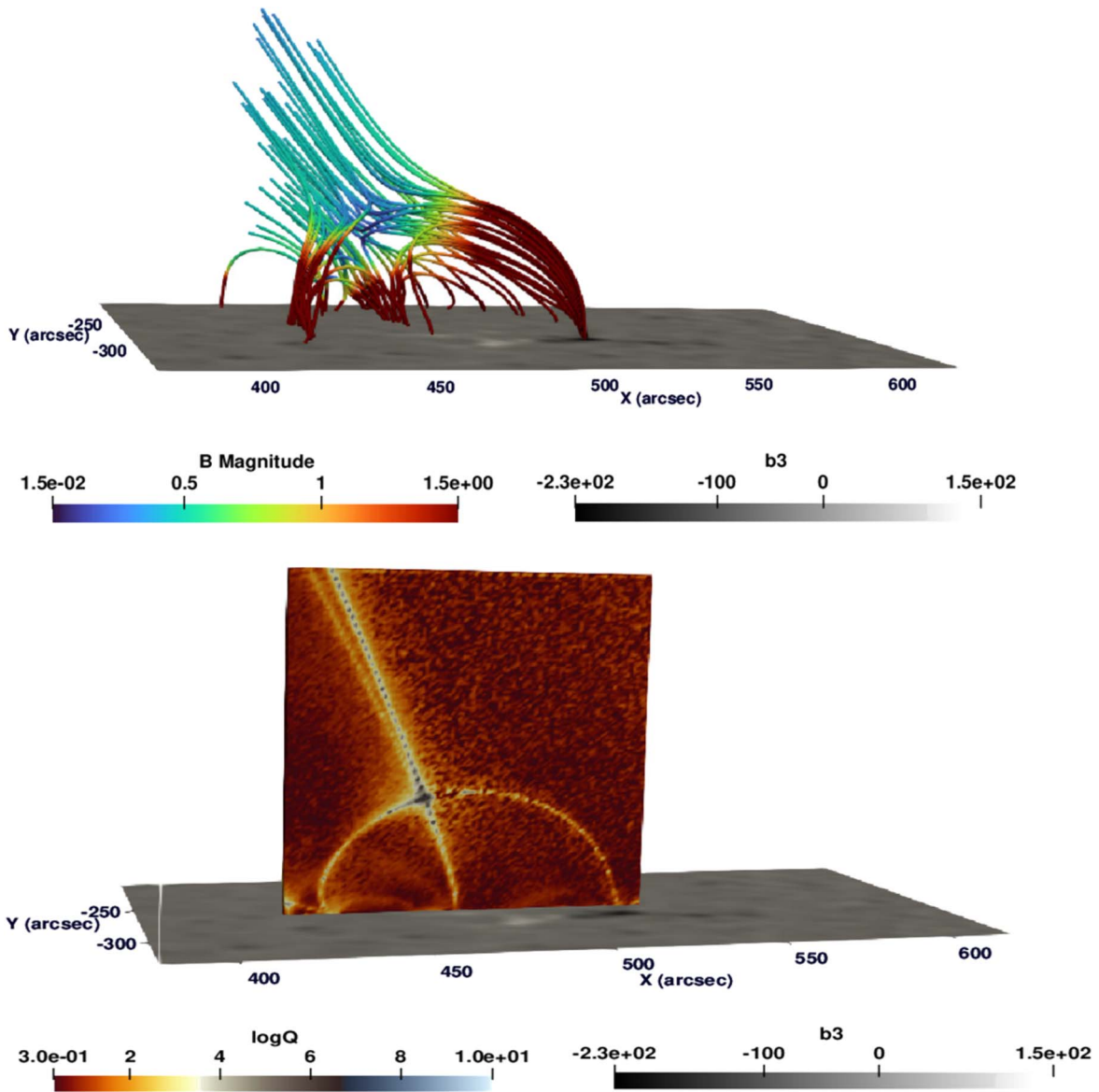
---

[10] http://amrvac.org

Figure 5. Top panel: extrapolated field lines in the ROI due to potential field extrapolation using MPI-AMRVAC. Bottom panel: surface representation of *Q* (squashing factor) distribution in the ROI resembling the extrapolated magnetic field structures. In both panels, b3 stands for the LOS component of vector magnetic field observed by SDO/HMI. b3 and *B*-magnitude are shown in the dimensionless code units used in MPI-AMRVAC. To convert these two quantities to units of gauss, the values shown in respective color bars should be multiplied by 2. In addition, the values shown in the color bar of *B*-magnitude are manually rescaled from exact values for better visualization. In addition, it is to be noted that the *x* and *y* coordinates are shown in the helioprojective Cartesian coordinate system to match with FOV of AIA observations.

originated from the same polarities (negative) and had their other footpoints in a magnetic polarity far from the feature of interest as shown in Figure 5 (top panel).

(II) *Magnetic nulls*. The extrapolated magnetic field topology was further analyzed using a range of methods (Poincaré index method and trilinear method) to compute the locations of magnetic nulls. But Olshevsky et al. (2020) suggested that use of the trilinear method is preferable for implementation to numerically simulated data with a Cartesian grid structure. Hence, we found a total of 49 nulls in the entire computational domain, of which 48 were in lower heights near the solar photosphere, while one is found in our ROI in the solar corona applying the trilinear method (Haynes & Parnell 2007; Olshevsky et al. 2020) in the Null_Finder[11] module. The exact

position of this null is found to be $x = 468''$ and $y = -240''$. Therefore, we confirm the presence of one magnetic null within ROI and hence provide evidence for a preferential topological feature associated with the onset of magnetic reconnection.

(III) *Quasi-separatrix layers (QSLs)*. In addition, we carried out an estimation for finding the presence of QSLs within the same domain (Guo et al. 2013; Yang et al. 2015) using the magnetic modeling codes[12] module. We calculated the squashing factor (Q), which is a function defined by Titov et al. (2002) to characterize QSLs. Basically, measurement of Q will determine the aspect ratio of the distorted ellipse exhibited owing to mapping of an elementary flux tube having its footpoint of positive (negative) polarity in an infinitesimal circular region to the footpoint of negative (positive) polarity

---

[11] https://github.com/FedericaChiti/Null_Finder/tree/v1.0.0

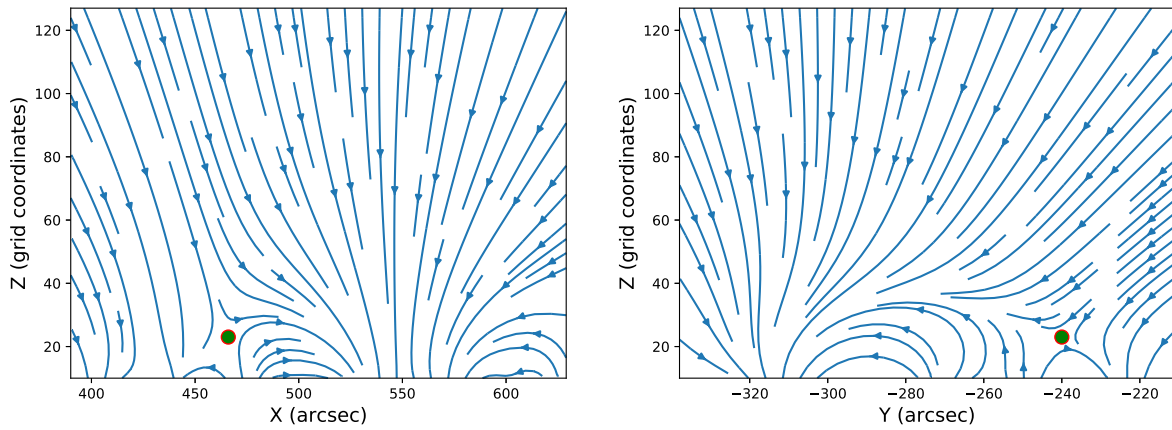[12] https://github.com/njuguoyang/magnetic_modeling_codes

Figure 6. Left panel: magnetic field streamlines and location of magnetic null, shown as a green sphere, are displayed while looking along the *Y*-direction. Right panel: magnetic field streamlines and location of magnetic null, shown as a green sphere, are displayed while looking against the *X*-direction. Spatial resolution along the *X*-direction is 1.46 Mm, and that along the *Y*- and *Z*-directions is 1.40 Mm. The null point (green sphere) found using the trilinear method (as shown in the right and left panels here) lies in the bottom part of the spine line at an exact location of $x = 468''$ and $y = -240''$. The x and y coordinates are shown in the helioprojective Cartesian coordinate system to match with the FOV of AIA observations.

sign, i.e., Q quantifies how much squashing is associated with the initial elementary region as a result of field-line mapping from one to the other footpoint (Baker et al. 2009).

Mathematically, QSLs are defined by $Q \gg 2$ (Titov et al. 2002; Baker et al. 2009). In our case, we found that Q had a maximum value as high as 10^{10} and the path traced by prominent positions of QSLs resembled spine fan topology (Figure 5; bottom panel), with a magnetic null at the intersection of the spine axis and the fan plane as evident in Figure 6. Hence, in 3D volume of the observed region, magnetic null is also present apart from enhanced Q value. Therefore, we consider that this region with QSLs, along with the presence of magnetic null, i.e., SLs, is favorably causing periodic reconnection (Thurgood et al. 2017, 2019).

The elongated cusp-shaped region of QSLs or SLs resembles the same feature evident in the EUV intensity (Figures 1–2) and DEM (Figure 4). The preexisting nonperiodic plasma upflows (Figure 3) during 18:56–19:03 UT transported mass from the left side of such magnetic field configuration to such a QSL (or SL) region on its top. The QSL region containing a magnetic null is the place where multiple reconnection took place after 19:10 UT, when heating occurred and intensity disturbances began to propagate toward the downward magnetic channel around 19:15 UT (see Figure 7 and related animation). Hence, the presence of heating at the top of the elongated cusp-shaped region in QSL or SL, which resemble the path followed by strong plasma flows moving toward the magnetic null situated at the intersection of spine axis and fan plane, provides conclusive evidence of the occurrence of magnetic reconnection in this ROI. Therefore, magnetic reconnection is established as the driving mechanism of the observed heating of the plasma and generation of PDs.

3.2. Nature of Propagating Disturbances

Successive bright and dark fronts were observed to propagate downward along the cusp-shaped region (which resembles now the QSL with a null in its lower segment) in the running-difference images of 304, 171, 193, and 131 Å (from top to bottom panel) in Figure 7 (see related animation also). The presence and propagation of these successive bright and dark fronts along field lines often suggest considering PDs as slow magnetoacoustic waves. But it is not straightforward, as

shown in some literature, as well as in this paper. Now the methods used for analysis of the observed PDs for searching propagation speeds and periodicity are described here in a sequential manner, along with their corresponding results. We used the method described in Yuan & Nakariakov (2012) to extract the distance–time maps. We took a straight slit S1 having a width of 5 pixels and a length of 13.20 Mm as shown in the top left panel of Figure 9 along the straight part of the considered magnetic geometry, along which PDs were noticed to propagate. Now it is clear that this elongated cusp-shaped region resembles the QSL in shape (bottom panel; Figure 5), and the PDs actually propagated in it downward. We estimated distance–time maps for normal intensity images. The distance–time diagrams for four wavelengths 304, 171, 193, and 131 Å are shown in top right panel of Figure 9. The bright ridges were seen in distance–time maps, which represent the propagation of PDs with time (as evident from tilted representation of those ridges) in all of these wavelengths.

Although we analyzed four AIA bandpasses (304, 171, 193, and 131 Å) only, the PDs were visible in all SDO/AIA bandpasses except 94 and 335 Å, as well as in different temperature ranges in DEM (as shown in the animation related to Figure 4). Therefore, we infer that the PDs are multi-temperature in nature. We used Si IV $\lambda1393.77$ optically thin lines (since the corresponding emission can be considered as the cooler counterpart of the EUV emissions observed via SDO/AIA, and almost similar to the formation temperature of AIA He II 304) to spectroscopically constrain the reconnection region.

We have taken Si IV line spectra from a few pixels around the red plus sign (as shown in the left panel of Figure 8) from each raster file. Basically, a raster scan is repeated at the red plus sign region at a time interval of 40 s, and we get a spectral line profile of Si IV over the reconnection region. Further, the averaged spectral profile is fitted by a single Gaussian to estimate line width variation in time. Then, we found that line width is subjected to a gradual rise (red line in the right panel of Figure 8) followed by a peak around 19:21 UT and a sharp decay after that (Figure 8, right panel). This time line is identical to the rise and fall of EM and temperature in the ROI, and overall the occurrence of the considered event. This line width increment is associated with the evolution of nonthermal
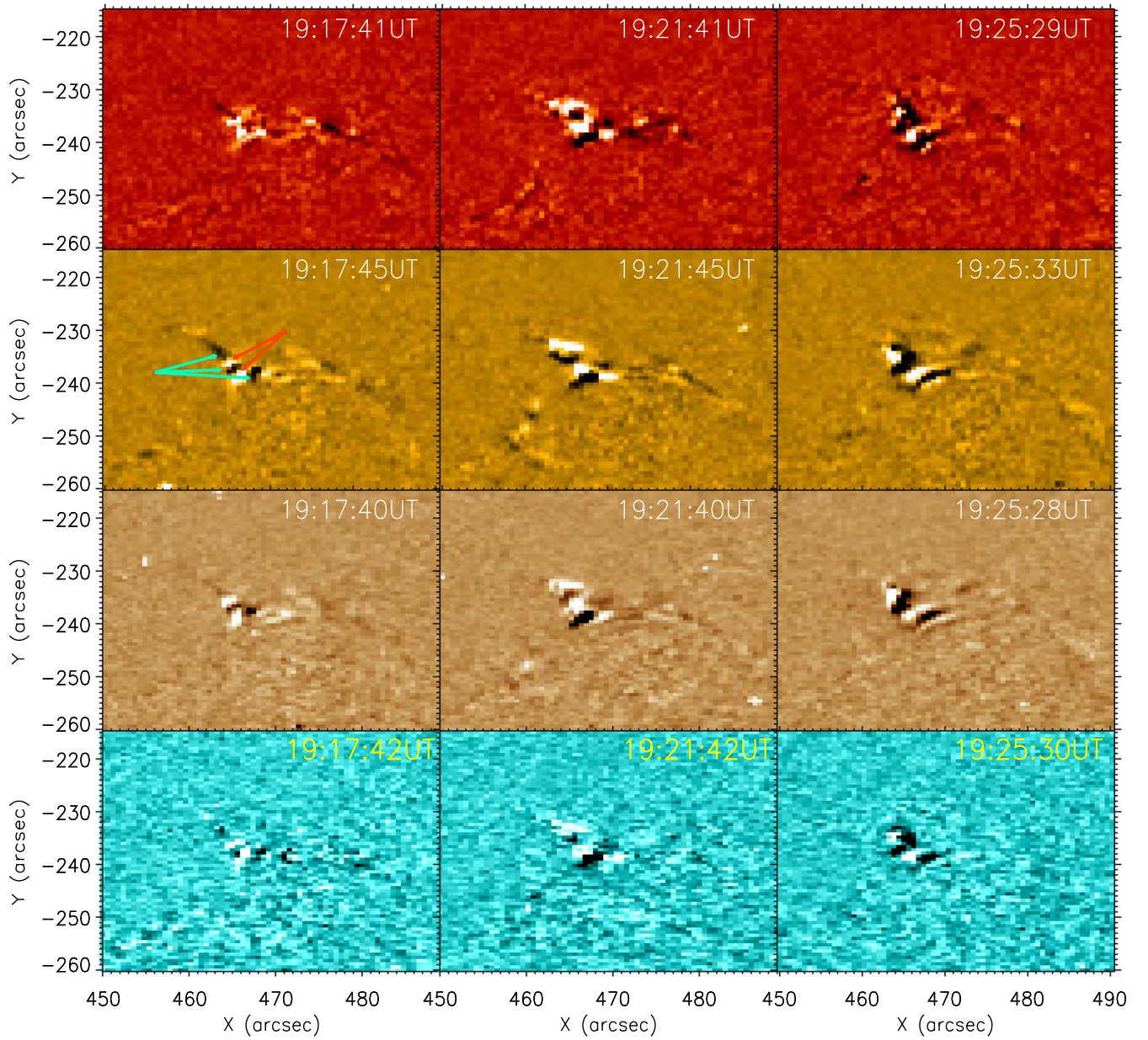
Figure 7. Running-difference images at wavelengths 304, 171, 193, and 131 Å (successively from top to bottom panel) for a time difference of 12 s covering different times within our considered temporal range showing successive bright and dark wavefronts propagating downward from the top of the elongated cusp-shaped region. Cyan arrows overplotted on the left panel of 171 images show dark fronts, whereas red arrows show bright ones. The full dynamics happening during the time duration from 19:03:21 UT to 19:32:57 UT, with temporal cadence being 12 s, is shown in the animation (only for 171 Å exhibited in the middle panel). The real-time animation duration is around 14 seconds.

(An animation of this figure is available.)

velocity (unresolved otherwise) of mass motion due to underlying turbulence (Doschek & Feldman 1977), quasiperiodic upflows, waves, or shocks (Tian et al. 2012; De Pontieu et al. 2015). Hence, the line width increment reconfirms the presence of plasma flows generated at the top of the elongated cusp-shaped region and thereafter propagated downward along the straight part of the cusp region.

3.2.1. Periodicity in Observed PDs

We extracted light curves exhibiting the evolution of intensity oscillations, for example, at a height of 6 Mm as denoted by horizontal magenta lines overplotted on distance–time maps shown in Figure 9. The corresponding normalized

light curves for four wavelengths, i.e., 304, 171, 193, and 131 Å, obtained by dividing the data points by their maximum values are shown in the top subpanel in the bottom panel of Figure 9. We performed wavelet analysis using a Morlet wavelet as a basis function to estimate the periodicity of the oscillations (Torrence & Compo 1998). The wavelet power spectra for different wavelength filters are shown in the bottommost subpanel in the bottom panel of Figure 9. The cross-hatched area on each wavelet power spectrum outlines the cone of influence (COI) where power is not considered reliable owing to edge effects. We have computed 95% local significance levels using the power-law model introduced by Auchère et al. (2016) and further used by Kayshap et al. (2020)
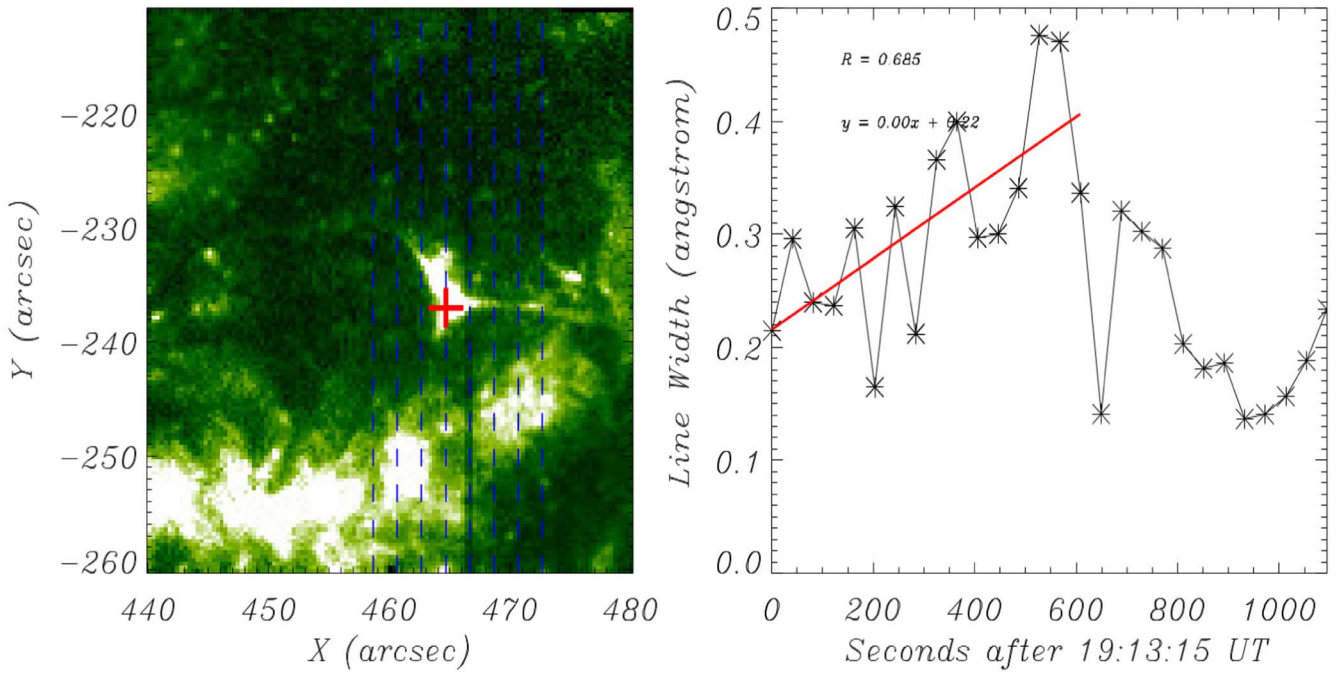
10

Figure 8. Left panel: eight slit positions corresponding to eight-step IRIS observations are shown as blue dashed lines overplotted on the IRIS/SJI C II λ1330 image. The red plus sign navigates the more specific region from where Si IV line spectra have been taken. Right panel: temporal evolution of line width in 1393.77 Å of the Si IV line in that region. The red line fit indicates an increasing trend of line width during the development of the reconnection event.

and Sangal et al. (2022). If ν is the Fourier frequency, the power-law equation (with A and C being constants) is given as

$$\sigma(\nu) = A\nu^s + C. \qquad (1)$$

We have fitted the fast Fourier transform (FFT) of each light curve with this power-law equation (as given above). Using the fitted curve as the background spectrum, we have estimated the 95% local significance level (Auchère et al. 2016).

In the subpanel between light curves and wavelet power spectra, the FFTs of the light curves are shown in black, and the global wavelet spectra (time average of the wavelet power spectrum) are shown in red. The fitted curves using the power-law equation are shown in blue, and 95% local significance levels are shown in green. If the global wavelet power is above these 95% local significance levels, only then is it considered significant (Torrence & Compo 1998). We have excluded the power that lies within COI and overplotted the 95% local significance contour on the wavelet power spectrum. Wavelet spectra have significant power within the range of 2–6 minutes, and the power is dominant at 4.28 minutes in all wave bands, i.e., 304, 171, 193, and 131 Å, as can be seen from the global power spectrum. This clearly elucidated the quasiperiodic nature of the PDs. To infer whether these quasiperiodic PDs are waves or flows, we estimated their speeds in four different wavelengths, i.e., 304, 171, 193, and 131 Å, as described in Section 3.2.2.

3.2.2. Propagation Speeds at Different Wavelengths

We used the surfing transform technique (Uritsky et al. 2013, 2021) to estimate the average speeds of quasiperiodic PDs at four different wavelengths, i.e., 304, 171, 193, and 131 Å. We calculated the surfing transform of the running-difference distance–time maps derived by a temporal difference of 12 s (as shown in Figure 10) for surfing speeds within a range of 20–250 km s^{-1}. We took the step size for increments

of surfing speeds during measurement to be 0.5 km s^{-1}. We inferred those surfing speeds as the average phase speed, which yielded the strongest surfing signal, as the signal met the resonance condition (for more details, see Uritsky et al. 2013). In those used maps shown in Figure 10, the resolution along the horizontal time axis is 2.36 s, and that along the vertical position axis is 0.09 Mm. Actually, the resolution on both axes, i.e., time and distance, were increased by 5 times that of AIA observations using the REBIN function in IDL, which gives an interpolation of the original maps. Basically, 1 pixel is subdivided into 5 subpixels for better visualization. Now in the surfing transform technique, during the error estimation, there are two major error sources: (a) the uncertainty in the peak determination, and (b) the uncertainty caused by the signal nonstationarity. The former depends on the length of the slit, the frequency of the oscillation, and the peak location (for more details, see Uritsky et al. 2013). The peak uncertainty (a) in our data is relatively small, about 1–2 km s^{-1}. The nonstationarity error (b) is substantially higher and considered as the main factor limiting the accuracy of the results. To estimate the nonstationarity error, we used the boxcar method. For each of four AIA channels, we computed the local surfing velocities for a set of 12.5-minute time intervals with a varying starting time, to evaluate the variability of the entire 25-minute time interval. It is to be noted that these local estimates are not statistically independent. But this is expected, as we are dealing with an uncertainty caused by nonstationarity, as the latter results from a combination of physical processes manifesting themselves as a long-term trend, with a significant autocorrelation time. It is this low-frequency process that makes the most significant contribution to the uncertainty. We used overlapping boxcar windows owing to the limited duration of studied solar events, but even if they were long enough to apply non-overlapping windows, the local estimates would not be statistically independent because of the physical origin of the
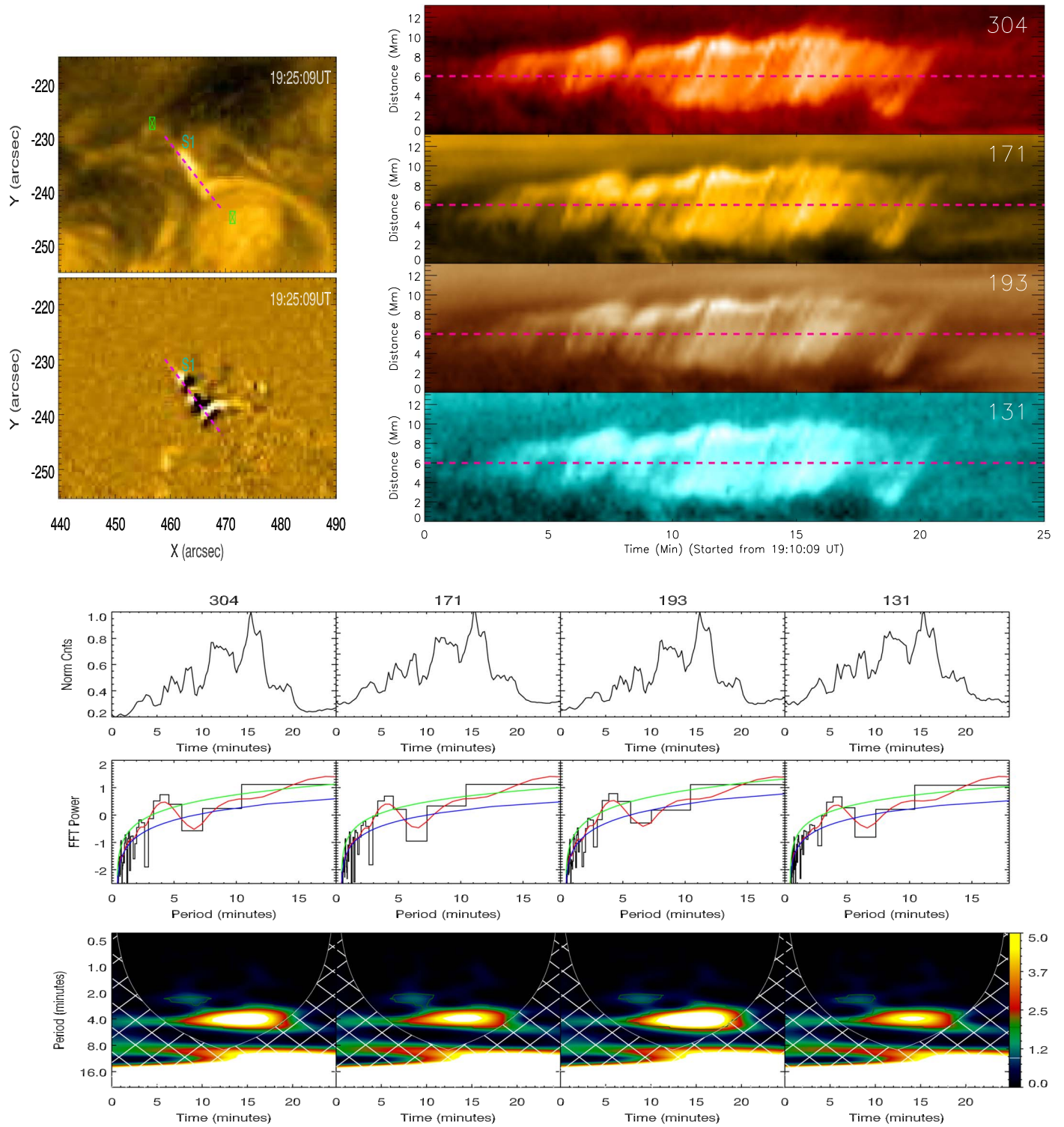
Figure 9. Top left panel: orientation of slit S1 overplotted as the magenta dashed line from a to b on the AIA 171 Å image (top: normal intensity; bottom: running difference of 12 s) having FOV $X = [440'', 490'']$, $Y = [-255'', -215'']$ covering the path along which PDs were found to propagate. Top right panel: derived distance–time maps at four different wavelengths, i.e., at 304, 171, 193, and 131 Å. Horizontal magenta lines show the height (6 Mm) at which the intensity time series were extracted for measurement of their periods. Bottom panel: extracted light curves after normalization (top); FFT of the light curves (black color) with global wavelet spectrum (red color), fitted curve using power law (blue color), and 95% significance level (green color) overplotted on it (middle); intensity wavelets with contour of significant power constrained by power law are shown for all four chosen wavelengths (bottom).

nonstationarity. We found that the boxcar-averaged corrected surfing speeds corresponding to the peaks of surfing signals, i.e., resonance of surfing signals as estimated accurately using parabolic fitting of surfing rms versus surfing speed profile (Uritsky et al. 2013), were 94.7 ± 4.0 km s^{-1} for the 304 Å passband, 90.1 ± 2.5 km s^{-1} for the 171 Å passband,
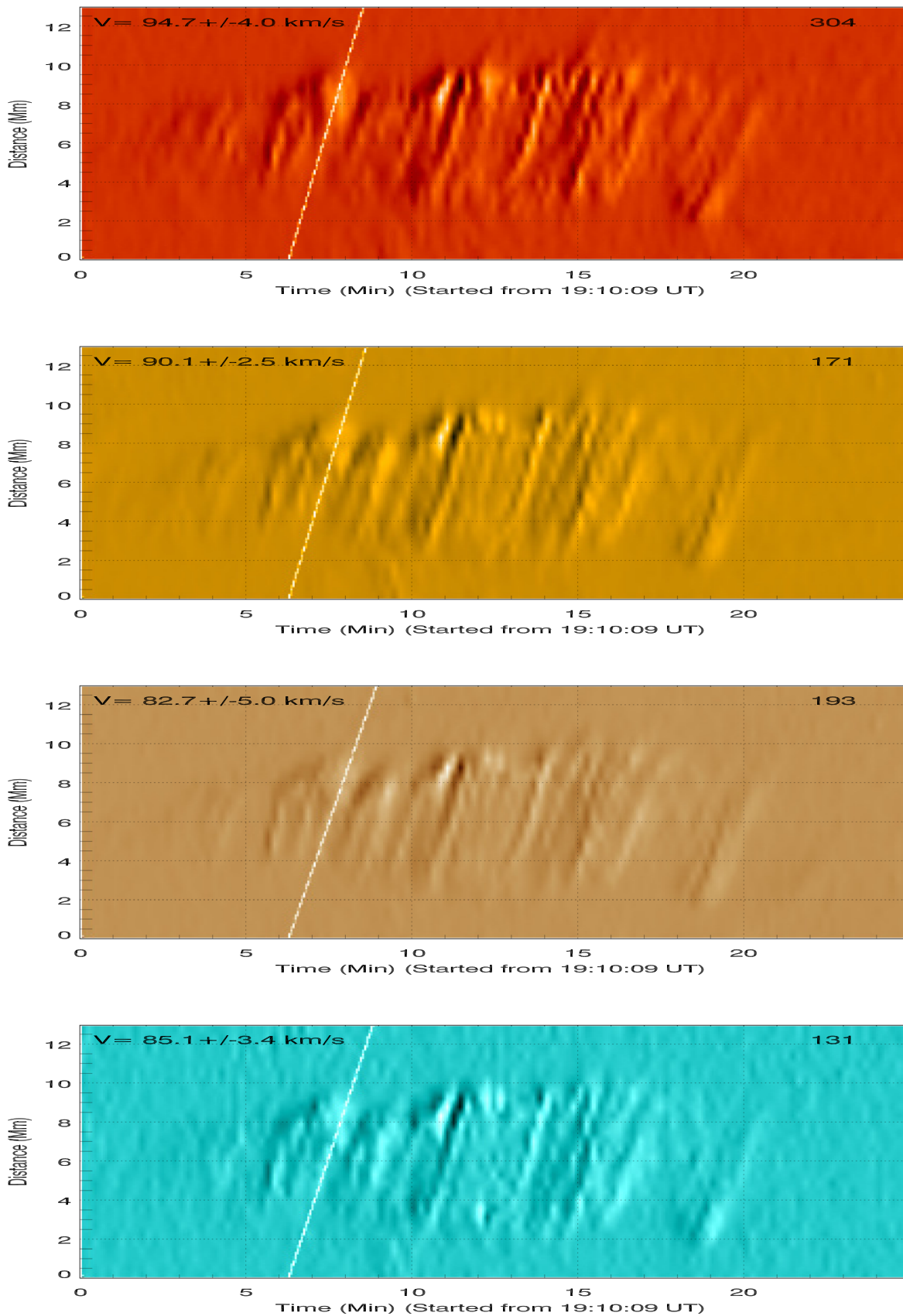
Figure 10. Running-difference distance–time maps at four different wavelengths, i.e., 304, 171, 193, and 131 Å (successively from top to bottom panel) estimated from the slit shown in the top left panel of Figure 9. Slopes shown as white straight lines overplotted on these maps correspond to the surfing speed necessary for the surfing signals to meet their resonance condition. The resolution along the time step axis is 2.36 s, and that along the position axis is 0.09 Mm, which are five times greater than the original resolutions of AIA observations. This transformation has been performed by using the REBIN function in IDL. The values of V basically suggest the surfing speed for which surfing signals reach their peak, and therefore these values are considered as propagation speeds of PDs.

82.7 ± 5.0 km s^{-1} for the 193 Å passband, and 85.1 ± 3.4 km s^{-1} for the 131 Å passband. It is to be noted that the abovementioned surfing rms is the rms of the pixel intensity. Its physical units are the same as the ones used in the processed AIA FITS files.

Now the coronal plasma is actually multithermal in nature, and the emission at various temperature is narrowband emission. In addition, emission at 304 Å wavelength is associated with an even cooler temperature (log T = 4.7) than the other three wavelength filters. Hence, keeping these in mind, it can be inferred that the plasma dynamics under consideration is truly multithermal in nature. In this circumstance, the estimated speeds at different wavelengths, i.e., at different temperatures, clearly suggest that these speeds are not scaled as $\sqrt{T}$ as expected for slow magnetoacoustic waves, where T stands for local temperature (Aschwanden 2004). For example, the ratio of theoretically predicted speeds at 304 and 171 Å is 0.27, but that for estimated speeds at 304 and 171 Å is within 0.98–1.13. If we consider the estimated speed at 304 Å as our reference speed and try to find the theoretically expected speeds, the speeds at other filters will be higher than that in 304 Å, which is not the case here. In general, the speeds are not increasing with the increment in the peak temperatures across different AIA wave bands and therefore are not scaled with $\sqrt{T}$. In addition to this, since we are using imaging observations that depend on density perturbations to probe the presence of any disturbances, the presence of Alfvén waves can be safely discarded, as it cannot be probed by perturbation in density because of its incompressible nature (Priest 2014). In addition, for fast waves, the propagation speeds are expected to be much larger (roughly of an order of 1000 km s^{-1} in the solar corona) than these speeds estimated using the surfing technique (Liu et al. 2011, 2012; Liu & Ofman 2014; Qu et al. 2017). Therefore, the PDs are essentially the flows, but certainly not the slow waves with phase speed scaled as $\sqrt{T}$ or any other form of waves like fast magnetoacoustic waves or Alfvén waves.

4. Discussion and Conclusion

Using SDO/AIA, we observed two narrow elongated curved features (magnetic flux tubes) to approach each other around 19:03 UT and thereafter merge with each other after a few moments. Prior to this merging, the nonperiodic plasma upflows from the left side of this region (as described in Figure 3) filled those particular strands that were merging. The thermal and magnetic measurements are consistent with magnetic reconnection in this elongated cusp-shaped region, which is essentially the QSL region more prone to the magnetic reconnection. The spectroscopic measurement of the Si IV line width increment is also consistent with the subsequent mass motion during the ongoing reconnection there. Intensity disturbances started to generate as a result of the inferred magnetic reconnection and propagated downward along the cusp part formed by merged field lines and thereafter predominantly along the extended right segment of field lines just after the merging.

As mentioned in the above summary, DEM analysis provided us a signature of the occurrence of heating in the top of the QSL region. This is linked with the signature of the occurrence of magnetic reconnection. The magnetic topology of the extrapolated field lines resembled closely the plasma emission structures as seen in SDO/AIA images. QSLs were found to be present in the ROI, resembling a spine and fan topology having a magnetic null at the intersection of the spine axis and the fan plane. The presence of magnetic null in the extrapolated field provides strong supporting evidence for the onset of magnetic reconnection in the ROI on the basis of favorable magnetic topology. Along with the magnetic null, QSLs are also preferential positions for the occurrence of magnetic reconnection, as those are the regions where magnetic field lines possess drastic changes in their connectivity, even though they are not purely discontinuous, i.e., oppositely directed to each other (Longcope & Strauss 1994; Priest & Démoulin 1995; Démoulin et al. 1997; Mandrini et al. 1997; Milano et al. 1999; Aulanier et al. 2005; Titov et al. 2008).

The PDs show a periodicity of about 4 minutes as estimated via wavelet analysis. As shown in Figure 7, the PDs were propagating as successive bright and dark fronts in running-difference images, which initially were suggestive of slow magnetoacoustic waves. However, this interpretation is not supported by the surfing transform analysis. If ϕ is an inclination angle of the coronal field lines along which the intensity disturbances propagate with the LOS, then the projected propagation speed of the disturbances, say, V_p, will be equal to $V_s \sin \phi$, where V_s is the actual speed (Wang et al. 2009). As the spatial region under consideration was far from the center of the disk, the projection effect came into the picture. Therefore, depending on the inclination angle ϕ, the projected propagation speed that we were estimating would be smaller than the actual speed. Nevertheless, if the disturbances were really slow-mode magnetoacoustic waves, the propagation speeds, even if they were smaller than the local sound speed, say, C_s, would follow $\sqrt{T}$ dependence as discussed in Aschwanden (2004). But the measurement of the propagation speed of PDs at different wavelengths, i.e., at different temperatures, exhibited the speeds that did not show $\sqrt{T}$ dependence. In addition, the presence of other forms of waves, e.g., fast magnetoacoustic waves or Alfvén waves, are discarded as explained in Section 3.2.2. Therefore, we describe these observed PDs as quasiperiodic plasma flows instead of the slow magnetoacoustic waves.

Various driving mechanisms were proposed recently to be associated with ubiquitous plasma flows since their discovery via Hinode/EIS observations (Del Zanna 2008; Tripathi et al. 2009, 2012; Srivastava et al. 2014). Chromopsheric evaporation as a result of reconnection due to flux emergence and braiding of field lines by random motions at the photospheric level, footpoints of active region loops subjected to an impulsive heating, evolution of large-scale reconnecting loops, etc., were carried forward as driving mechanisms of those outflows (Del Zanna 2008; Hara et al. 2008; Harra et al. 2008). One possible mechanism behind the generation of periodic reconnection outflows at a 3D magnetic null is oscillatory reconnection (Thurgood et al. 2017), although the expected periodicity of this mechanism in the corona is not yet well constrained (Thurgood et al. 2019). Along with the existence of a null point resulting in magnetic reconnection, generation of plasma flows in ARs is also related to the presence of QSLs and the occurrence of reconnection there as first proposed by Baker et al. (2009). Using Hinode/EIS, van Driel-Gesztelyi et al. (2012) observed AR-related plasma outflows and measured their speeds. They performed magnetic field extrapolations of AR and confirmed cospatiality of outflows with QSL locations, including the separatrix of a magnetic null. Démoulin et al.

(2013) found that the coronal plasma upflows from the edges of AR 10978 were thin, fan-like structures rooted in QSLs between high-pressure AR loops and lower-pressure loops in the neighborhood. In addition, Mandrini et al. (2015) reported that AR plasma upflows observed by EIS and QSLs located by analyzing extrapolated field lines were found to evolve in parallel, both temporarily and spatially. Baker et al. (2017, 2021) had carried out similar analysis and interpretation of the driver of plasma upflows in ARs. Hence, it has been inferred that strong and dominant QSLs (with or without magnetic nulls) are the preferential positions for accumulation of strong current and the occurrence of magnetic reconnection resulting in observed plasma outflows in solar ARs.

In this paper, we analyzed multiwavelength imaging observations of quasiperiodic plasma flows and found the presence of a magnetic null, as well as dominant QSLs resembling the path followed by the strong outflows. We observed the flow to be asymmetrically propagating, as it was mostly propagating along the right segment of an inverted Y-shaped magnetic channel as seen in the plane-of-sky (2D) AIA images. We conjecture that the presence of field lines having larger strength was leading to dominant movement of plasma flows in that direction as compared to the relatively weaker field lines in the left segment. In this work, in addition to locating the presence of a magnetic null in the ROI and matching the position of QSLs with strong plasma flows, we examined heating in the top of the elongated cusp-shaped region, where the bundles of field lines or flux tubes were merging with each other, via DEM analysis, and therefore provided detailed evidence of magnetic reconnection. In addition, since we implemented the surfing transform method to compare the propagation speeds at different wavelengths or different temperatures, it came out that the speeds at four different wavelengths, i.e., at different temperatures, were not scaled as $\sqrt{T}$ and therefore provided confirmation about our interpretation of the plasma flows instead of slow magnetoacoustic waves. In addition, we performed wavelet analysis to examine the periodicities in the PDs. We found quasiperiodicity of about 4 minutes associated with these PDs. Therefore, we infer that the reconnection that was acting as a driver of these quasiperiodic plasma flows may be taking place periodically in QSL or SL regions (akin to elongated cusp-shaped regions as seen in AIA images). The bundle of field lines or flux tubes might be undergoing repetitive merging due to changes in pressure gradient between them. The faint plasma upflows (discussed in Figure 3) that were observed to propagate through various channels almost repetitively might have established some additional plasma pressure and therefore total pressure that may lead to rightward movement of left field-line bundles, resulting in repetitive merging of it with the bundle of field lines on the right side and hence in periodic reconnection. In addition, the in-phase fluctuations of EM and DEM-weighted temperature (as shown in the bottom panel of Figure 4) may be suggesting that quasiperiodic flows are produced by intermittent heating during the reconnection process. We present a detailed physical picture in this paper regarding magnetic-reconnection-generated quasiperiodic plasma flows using the analyzed observations. We anticipate that new upcoming high-resolution and high-cadence imaging observations will confirm and elaborate such dynamical plasma processes at different QSLs/SLs in various parts of the solar corona.

In previous literature, in general, the quasiperiodic intensity (and thus density) fluctuations in the distance–time maps, as well as light curves, were demonstrated as the signature of magnetoacoustic waves (e.g., Ofman et al. 1997; De Moortel et al. 2000; Banerjee et al. 2009; Marsh et al. 2009; Krishna Prasad et al. 2011; Stenborg et al. 2011; Gupta et al. 2012; Kumar et al. 2013, 2015; Nisticò et al. 2017). We are not in disagreement with those physical scenarios of magnetoacoustic waves, and they must remain valid in such cases of plasma dynamics seen in the localized solar atmosphere. However, in this paper, using the theoretical argument of $\sqrt{T}$ dependence of propagation speed along with application of the surfing technique for stringent analyses of speeds, we find that if $\sqrt{T}$ dependence of phase speeds does not hold true for any specific physical dynamics and the estimated phase speeds are much less than the speeds expected for fast magnetoacoustic waves, the presence of quasiperiodic intensity fluctuations or successive bright and dark tilted ridges in distance–time maps can be a signature of quasiperiodic flows instead of magnetoacoustic waves. Hence, through this work, we put forward the fact that there will not always be a one-to-one correspondence between the presence of successive bright or dark ridges in distance–time map and a signature of magnetoacoustic waves (Su et al. 2012; Pucci et al. 2014). We suggest that similar observables can be linked with different physical processes at any particular epoch of time in the localized solar atmosphere; thus, caution should be taken in the form of stringent analysis before making physical interpretations. Although the waves and flows can also coexist in many cases, here our detailed analyses demonstrate alone the origin of quasiperiodic plasma flows due to reconnection in the QSL/SL above the magnetic null in the localized corona.

ORCID iDs

Abhishek K. Srivastava ● https://orcid.org/0000-0002-1641-1539
K. Sangal ● https://orcid.org/0000-0003-0596-5277
Pradeep Kayshap ● https://orcid.org/0000-0002-1509-3970
Yang Guo ● https://orcid.org/0000-0002-9293-8439

David I Pontin ⬤ https://orcid.org/0000-0002-1089-9270
Vadim M. Uritsky ⬤ https://orcid.org/0000-0002-5871-6605
Leon Ofman ⬤ https://orcid.org/0000-0003-0602-6693
Tongjiang Wang ⬤ https://orcid.org/0000-0003-0053-1146
Ding Yuan ⬤ https://orcid.org/0000-0002-9514-6402

References

Aly, J. J., & Amari, T. 1989, A&A, 221, 287
Aschwanden, M. J 2004, Physics of the Solar Corona. An Introduction (Berlin: Springer)
Auchère, F., Froment, C., Bocchialini, K., Buchlin, E., & Solomon, J. 2016, ApJ, 825, 110
Aulanier, G., Pariat, E., & Démoulin, P. 2005, A&A, 444, 961
Baker, D., Janvier, M., Démoulin, P., & Mandrini, C. H. 2017, SoPh, 292, 46
Baker, D., Mihailescu, T., Démoulin, P., et al. 2021, SoPh, 296, 103
Baker, D., van Driel-Gesztelyi, L., Mandrini, C. H., Démoulin, P., & Murray, M. J. 2009, ApJ, 705, 926
Banerjee, D., O'Shea, E., Doyle, J. G., & Goossens, M. 2001, A&A, 377, 691
Banerjee, D., Teriaca, L., Gupta, G. R., et al. 2009, A&A, 499, L29
Baty, H. 2000, A&A, 353, 1074
Chen, Y., Tian, H., Huang, Z., Peter, H., & Samanta, T. 2019, ApJ, 873, 79
Chen, Z. Z., Fu, H. S., Liu, C. M., et al. 2019, GeoRL, 46, 5698
Cheung, M. C. M., Boerner, P., Schrijver, C. J., et al. 2015, ApJ, 807, 143
Chiu, Y. T., & Hilton, H. H. 1977, ApJ, 212, 873
Cho, K.-S., Cho, I.-H., Madjarska, M. S., et al. 2021, ApJ, 909, 202
Dadashi, N., Teriaca, L., & Solanki, S. K. 2011, A&A, 534, A90
De Moortel, I., Ireland, J., & Walsh, R. W. 2000, A&A, 355, L23
De Pontieu, B., McIntosh, S., Martinez-Sykora, J., Peter, H., & Pereira, T. M. D. 2015, ApJL, 799, L12
De Pontieu, B., & McIntosh, S. W. 2010, ApJ, 722, 1013
De Pontieu, B., McIntosh, S. W., Carlsson, M., et al. 2011, Sci, 331, 55
De Pontieu, B., Title, A. M., Lemen, J. R., et al. 2014, SoPh, 289, 2733
DeForest, C. E., & Gurman, J. B. 1998, ApJL, 501, L217
Del Zanna, G. 2008, A&A, 481, L49
Démoulin, P., Bagala, L. G., Mandrini, C. H., Henoux, J. C., & Rovira, M. G. 1997, A&A, 325, 305
Démoulin, P., Baker, D., Mandrini, C. H., & van Driel-Gesztelyi, L. 2013, SoPh, 283, 341
Doschek, G. A., & Feldman, U. 1977, ApJL, 212, L143
Forbes, T. G. 2000, AdSpR, 26, 549
Freeland, S. L., & Handy, B. N. 1998, SoPh, 182, 497
Fu, H. S., Vaivads, A., Khotyaintsev, Y. V., et al. 2017, GeoRL, 44, 37
Gaizauskas, V., Mandrini, C. H., Demoulin, P., Luoni, M. L., & Rovira, M. G. 1998, A&A, 332, 353
Galsgaard, K., Priest, E. R., & Nordlund, Å. 2000, SoPh, 193, 1
Gary, G. A., & Hagyard, M. J. 1990, SoPh, 126, 21
Greene, J. M. 1988, JGR, 93, 8583
Guennou, C., Auchère, F., Soubrié, E., et al. 2012, ApJS, 203, 26
Guo, Y., Cheng, X., & Ding, M. 2017, ScChD, 60, 1408
Guo, Y., Ding, M. D., Cheng, X., Zhao, J., & Pariat, E. 2013, ApJ, 779, 157
Gupta, G. R., Teriaca, L., Marsch, E., Solanki, S. K., & Banerjee, D. 2012, A&A, 546, A93
Hahm, T. S., & Kulsrud, R. M. 1985, PhFl, 28, 2412
Hara, H., Watanabe, T., Harra, L. K., et al. 2008, ApJL, 678, L67
Harra, L. K., Sakao, T., Mandrini, C. H., et al. 2008, ApJL, 676, L147
Haynes, A. L., & Parnell, C. E. 2007, PhPl, 14, 082107
Heyvaerts, J., & Priest, E. R. 1983, A&A, 117, 220
Ionson, J. A. 1978, ApJ, 226, 650
Kayshap, P., Banerjee, D., & Srivastava, A. K. 2015, SoPh, 290, 2889
Kayshap, P., Srivastava, A. K., Tiwari, S. K., Jelínek, P., & Mathioudakis, M. 2020, A&A, 634, A63
Keppens, R., Meliani, Z., van Marle, A. J., et al. 2012, JCoPh, 231, 718
Keppens, R., Teunissen, J., Xia, C., & Porth, O. 2021, Comput. & Math. with Appl., 81, 316
Kiddie, G., De Moortel, I., Del Zanna, G., McIntosh, S. W., & Whittaker, I. 2012, SoPh, 279, 427
Krishna Prasad, S., Banerjee, D., & Gupta, G. R. 2011, A&A, 528, L4
Krishna Prasad, S., Banerjee, D., Van Doorsselaere, T., & Singh, J. 2012, A&A, 546, A50
Kumar, P., Innes, D. E., & Inhester, B. 2013, ApJL, 779, L7
Kumar, P., Nakariakov, V. M., & Cho, K.-S. 2015, ApJ, 804, 4
Lau, Y.-T., & Finn, J. M. 1990, ApJ, 350, 672
Leka, K. D., Barnes, G., Crouch, A. D., et al. 2009, SoPh, 260, 83
Lemen, J. R., Title, A. M., Akin, D. J., et al. 2012, SoPh, 275, 17

Li, D., Ning, Z., & Su, Y. 2016, Ap&SS, 361, 301
Li, L., Zhang, J., Peter, H., et al. 2018, ApJL, 868, L33
Liu, C. M., Fu, H. S., Cao, D., Xu, Y., & Divin, A. 2018, ApJ, 860, 128
Liu, W., & Ofman, L. 2014, SoPh, 289, 3233
Liu, W., Ofman, L., Nitta, N. V., et al. 2012, ApJ, 753, 52
Liu, W., Title, A. M., Zhao, J., et al. 2011, ApJL, 736, L13
Longcope, D. W., & Strauss, H. R. 1994, ApJ, 437, 851
Mandrini, C. H., Baker, D., Démoulin, P., et al. 2015, ApJ, 809, 73
Mandrini, C. H., DÉmoulin, P., BagalÁ, L. G., et al. 1997, SoPh, 174, 229
Marsh, M. S., Walsh, R. W., & Plunkett, S. 2009, ApJ, 697, 1674
McIntosh, S. W., Innes, D. E., de Pontieu, B., & Leamon, R. J. 2010, A&A, 510, L2
Metcalf, T. R. 1994, SoPh, 155, 235
Metcalf, T. R., Leka, K. D., Barnes, G., et al. 2006, SoPh, 237, 267
Milano, L. J., Dmitruk, P., Mandrini, C. H., Gómez, D. O., & Démoulin, P. 1999, ApJ, 521, 889
Ning, Z., & Guo, Y. 2014, ApJ, 794, 79
Nisticò, G., Polito, V., Nakariakov, V. M., & Del Zanna, G. 2017, A&A, 600, A37
Ofman, L., Romoli, M., Davila, J. M., et al. 1997, in Fifth SOHO Workshop: The Corona and Solar Wind Near Minimum Activity, 404 (Paris: ESA), 571
Ofman, L., Wang, T. J., & Davila, J. M. 2012, ApJ, 754, 111
Olshevsky, V., Pontin, D. I., Williams, B., et al. 2020, A&A, 644, A150
O'Shea, E., Banerjee, D., & Doyle, J. G. 2007, A&A, 463, 713
Parker, E. N. 1988, ApJ, 330, 474
Parnell, C. E., Neukirch, T., Smith, J. M., & Priest, E. R. 1997, GApFD, 84, 245
Parnell, C. E., Smith, J. M., Neukirch, T., & Priest, E. R. 1996, PhPl, 3, 759
Pontin, D. I., & Priest, E. R. 2022, LRSP, 19, 1
Porth, O., Xia, C., Hendrix, T., Moschou, S. P., & Keppens, R. 2014, ApJS, 214, 4
Priest, E. 2014, Magnetohydrodynamics of the Sun (Cambridge: Cambridge Univ. Press)
Priest, E., & Forbes, T. 2007, Magnetic Reconnection (Cambridge: Cambridge Univ. Press)
Priest, E. R. 1996, in ASP Conf. Ser. 111, Magnetic Reconnection in the Solar Atmosphere, ed. R. D. Bentley & J. T. Mariska (San Francisco, CA: ASP), 331
Priest, E. R., & Démoulin, P. 1995, JGR, 100, 23443
Priest, E. R., & Titov, V. S. 1996, RSPTA, 354, 2951
Pucci, S., Poletto, G., Sterling, A. C., & Romoli, M. 2014, ApJ, 793, 86
Qu, Z. N., Jiang, L. Q., & Chen, S. L. 2017, ApJ, 851, 41
Rao, Y. K., Srivastava, A. K., Kayshap, P., Wilhelm, K., & Dwivedi, B. N. 2019, ApJ, 874, 56
Sangal, K., Srivastava, A. K., Kayshap, P., et al. 2022, MNRAS, 517, 458
Scherrer, P. H., Schou, J., Bush, R. I., et al. 2012, SoPh, 275, 207
Schou, J., Scherrer, P. H., Bush, R. I., et al. 2012, SoPh, 275, 229
Srivastava, A. K., Konkol, P., Murawski, K., Dwivedi, B. N., & Mohan, A. 2014, SoPh, 289, 4501
Srivastava, A. K., Mishra, S. K., & Jelínek, P. 2021, ApJ, 920, 18
Srivastava, A. K., Mishra, S. K., Jelínek, P., et al. 2019, ApJ, 887, 137
Srivastava, A. K., Rao, Y. K., Konkol, P., et al. 2020, ApJ, 894, 155
Srivastava, A. K., Shetye, J., Murawski, K., et al. 2017, NatSR, 7, 43147
Stenborg, G., Marsch, E., Vourlidas, A., Howard, R., & Baldwin, K. 2011, A&A, 526, A58
Su, J. T., Shen, Y. D., & Liu, Y. 2012, ApJ, 754, 43
Thurgood, J. O., Pontin, D. I., & McLaughlin, J. A. 2017, ApJ, 844, 2
Thurgood, J. O., Pontin, D. I., & McLaughlin, J. A. 2019, A&A, 621, A106
Tian, H., McIntosh, S. W., & De Pontieu, B. 2011, ApJL, 727, L37
Tian, H., McIntosh, S. W., Wang, T., et al. 2012, ApJ, 759, 144
Titov, V. S., Hornig, G., & Démoulin, P. 2002, JGRA, 107, 1164
Titov, V. S., Mikic, Z., Linker, J. A., & Lionello, R. 2008, ApJ, 675, 1614
Torrence, C., & Compo, G. P. 1998, BAMS, 79, 61
Tripathi, D., Mason, H. E., Del Zanna, G., & Bradshaw, S. 2012, ApJL, 754, L4
Tripathi, D., Mason, H. E., Dwivedi, B. N., del Zanna, G., & Young, P. R. 2009, ApJ, 694, 1256
Uritsky, V. M., Davila, J. M., Viall, N. M., & Ofman, L. 2013, ApJ, 778, 26
Uritsky, V. M., DeForest, C. E., Karpen, J. T., et al. 2021, ApJ, 907, 1
van Ballegooijen, A. A., Asgari-Targhi, M., Cranmer, S. R., & DeLuca, E. E. 2011, ApJ, 736, 3
van der Holst, B., Keppens, R., Meliani, Z., et al. 2012, MPI-AMRVAC: MPI-Adaptive Mesh Refinement-Versatile Advection Code, Astrophysics Source Code Library, ascl:1208.014
Van Doorsselaere, T., Srivastava, A. K., Antolin, P., et al. 2020, SSRv, 216, 140

van Driel-Gesztelyi, L., Culhane, J. L., Baker, D., et al. 2012, SoPh, 281, 237
Vekstein, G. 2017, JPlPh, 83, 205830501
Vekstein, G., Priest, E. R., & Amari, T. 1991, A&A, 243, 492
Wang, H. 1997, SoPh, 174, 265
Wang, T. J., Ofman, L., Davila, J. M., & Mariska, J. T. 2009, A&A, 503, L25
Wiegelmann, T., Inhester, B., & Sakurai, T. 2006, SoPh, 233, 215
Xia, C., Teunissen, J., El Mellah, I., Chané, E., & Keppens, R. 2018, ApJS, 234, 30
Yang, K., Guo, Y., & Ding, M. D. 2015, ApJ, 806, 171
Yuan, D., & Nakariakov, V. M. 2012, A&A, 543, A9